2024 IEEE International Conference on Robotics and Automation (ICRA 2024)
May 13-17, 2024. Yokohama, Japan

Microrobotic Flight Enabled by Ultralight Ion Thrusters with High Thrust-to-Weight Ratio and Low Fabrication Cost

Yang Gu[1,*], Xianfa Cai[1,*], Khadga Thakuri[2], Wenyu Yang[3], Yufeng Guo[1] and Wei Li[1,4]

***Abstract*—Flying microrobots have garnered growing research interest owing to their technological intricacies and suitability for various applications leveraging miniaturized size. Electrohydrodynamic (EHD) thrust offers advantages by generating propulsion without moving parts, but real-world use is limited by insufficient thrust generation, manufacturing challenges, fragility, and cost. This work presents the design and development of an optimized ion-propelled flying microrobot that excels in low weight, high thrust-to-weight ratio, and cost efficiency. Regarding design, multiphysics simulations guided structural optimization to increase thrust while decreasing weight. For materials, metal-coated polyethylene terephthalate (PET) film was selected to leverage the combined merits of metal conductivity and polymer flexibility, light weight, and low cost, enabling further weight reduction, easy assembly, robustness, and cost-effectiveness. Various experiments, including voltage-current measurements, ionic wind speed, thrust quantification, and airflow visualization, directed design refinements and validated performance. Through structural optimization, the maximum wind speed attained 2.25 m/s. Flight demonstrations with payloads evidenced the microrobot can stably fly at an inherent 16 mg weight while carrying an additional 72 mg load, achieving a record 5.5 thrust-to-weight ratio. These results open possibilities to incorporate microelectronics, enabling autonomous flight functionality.**

I. Introduction

Flying microrobots involve small-scale aerial vehicles designed to operate in confined spaces, perform complex tasks, and navigate challenging environments with high maneuverability [1-3]. With advances in precision manufacturing and intelligent control [4], flying microrobots are receiving substantial attention and development across fields like disaster rescue, surveillance, infrastructure monitoring and planetary exploration [5]. Compared to large and medium-sized aircraft, flying microrobots [6-9] enable unique application scenarios, but present challenges including miniaturizing propulsion systems, insufficient onboard power, manufacturing and assembly complexity, and complex control needs. Currently, there are mainly three types of flying microrobots that can be categorized based on different principles: micro-rotorcrafts [10-12], flapping wings robots [13-15], and ion-propelled flying robots [16-18]. Micro-rotorcrafts rely on electromagnetic motors, which have substantial weight for their sizes; moreover, enough space must be allocated to accommodate these components, posing a potential obstacle to miniaturization. Flapping-wings microrobots require the installation of bionic flapping-wings as the micro-actuators, as well as embedded precise sensors and control system to enable insect-like flight [3,13-15]. The wings must frequently flap at high speeds to generate lift, imposing cyclic stress on components that may accumulate damage over time.

Ion-propelled flying microrobots have a distinctive advantage over other types of flying microrobots in that they operate without the need for any moving parts. This eliminates the constraints of space and payload requirements associated with such components, enabling a streamlined design and allowing for silent operation without any high-speed motion. The propulsion of ion-propelled flying microrobots relies on electrohydrodynamic (EHD) mechanisms generated by corona discharge, as depicted in Fig. 1(a). By applying a potential difference between the emitter and collector, the air molecules near the emitter can be ionized, and the resultant ions, driven by the electric field, impart momentum to the neutral air molecules, creating a macroscopic ionic wind effect [18]. The stable and controlled flight of these microrobots can be achieved by simply adjusting the supply voltage to regulate the strength of the ionic wind, ensuring reliable and directional movement.

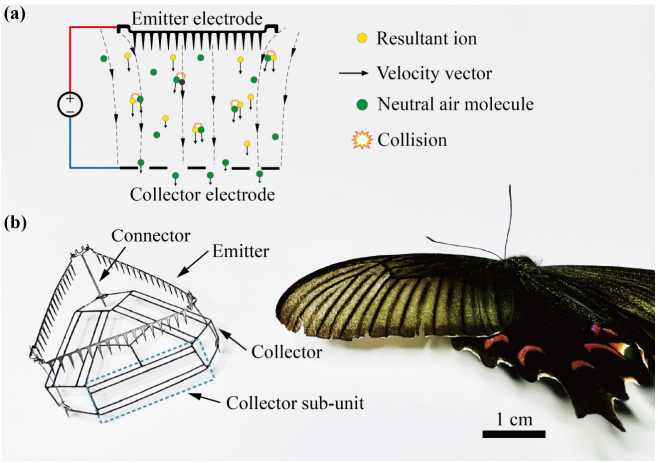

Fig. 1. (a) Schematic diagram of the principle of ionic propulsion. (b) Assembled ion-propelled flying microrobot, weighing 16 mg, beside a butterfly.

The current challenge for micro ion-propelled flying robots lies mainly in substantially improving manufacturing and assembly efficiency, while strikingly increasing the thrust-to-weight ratio [17]. The primary factor constraining the performance of ion-propelled flying microrobots is their low magnitude of effective thrust [20-22]. The main reason is

*These authors contributed equally to the work.
[1]College of Integrated Circuit Science and Engineering, Nanjing University of Posts and Telecommunications, Nanjing, Jiangsu, 210023, China
[2]Department of Physics, University of Vermont, Burlington, VT 05405, USA
[3]School of Mechanical Science and Technology, Huazhong University of Science and Technology, Wuhan, Hubei, 430074, China
[4]Department of Mechanical Engineering, University of Vermont, Burlington, VT 05405, USA
yfguo@njupt.edu.cn; wei.li@njupt.edu.cn

insufficient optimization of the flying microrobot's structure and ineffective utilization of the ionic wind. When the performance of corona discharge is not fully utilized, it becomes difficult to further improve the thrust-to-weight ratio. Currently, reported thrust-to-weight ratios of ion-propelled flying microrobots range from 1 to 2.5 [16-18], which is unfavorable for stable flight with higher payloads (i.e., sensors, batteries, cameras, etc.). Additionally, state-of-the-art ion-propelled flying microrobots are made either from microfabricated silicon-on-insulator wafers using cleanroom facilities [9] or from various metal films [16, 17] using precision laser manufacturing. Therefore, present mass production methods for ion-propelled flying microrobots may require extensive manufacturing and assembly times, high costs, and specialized high-end equipment.

In this paper, we report on the design, simulation, fabrication, calibration and testing of an ultra-low weight, record-high thrust-to-weight ratio, low-cost ion-propelled flying microrobot (Fig. 1(b)). The microrobot is fabricated from 50 μm thick aluminum-coated polyethylene terephthalate (Al-PET) and 100 μm thick polyvinyl chloride (PVC) thin film cut by a household DIY cutting machine. The materials and manufacturing process enhance the robustness and flexibility of the developed flying microrobot, while reducing manufacturing time, cost, and assembly complexity. Furthermore, finite element analysis (FEA) optimizes the structural design for airflow performance, resulting in an effective combination of light weight and high thrust. The FEA results are experimentally verified, and the performance of the designed ionic wind thrusters is analyzed through visualization. The 16 mg flying microrobot achieves a maximum all-up weight (AUW) capacity of 88 mg. The loaded flight experiments demonstrate the microrobot can attain a record-high 5.5 thrust-to-weight ratio, providing insights to optimize performance and inform future ion-propelled microrobot development.

II. Structure Design

Ion-propelled flying microrobot harnesses the propulsive force through the mechanism of EHD, which explores the combination of electrostatics and laminar flow with the charged ions. The EHD force can be expressed as [16]:

$$F = \int \rho_e E dV = \frac{Id}{\mu} , \tag{1}$$

where ρ_e is the charge density, E is the electric field, V is the supply voltage, I is the ion current, d is the distance between electrodes, and μ is the ion mobility in the air.

According to the Townsend discharge, the voltage-current relationship can be experimentally derived as [23, 24]:

$$I = CV(V - V_0) , \tag{2}$$

$$C = \frac{C'\mu}{d^2} , \tag{3}$$

where V_0 is the corona inception voltage, and C and C' are constants related to electrode geometry. Derived from (1), (2), and (3), the EHD force is [25]:

$$F = \frac{C'V(V - V_0)}{d} . \tag{4}$$

Thus, to maximize EHD force, the supply voltage V can approach the breakdown voltage V_B (i.e., $V \approx V_B$). Per Paschen's law, V_B is [26]:

$$V_B = \frac{Bpd}{\ln(Apd) - \ln\left[\ln\left(1 + \frac{1}{\gamma}\right)\right]} , \tag{5}$$

where p is air pressure, γ is the secondary-electron-emission coefficient of the cathode, and A, B are constants determined experimentally (in air, A=15, B=365). Additionally, the corona onset potential between a wire and a plane is [8]:

$$V_0 = m_v g_0 R\left(1 + \frac{0.301}{\sqrt{R}}\right)\ln\left(\frac{2d}{R}\right) , \tag{6}$$

where m_v is a coefficient determined by the surface properties of the emitter (e.g., m_v=1 for a smooth polished wire), g_0 is the breakdown field strength (e.g., 30000 V/cm for the air), and R is the wire radius. From (4), (5) and (6), the maximum EHD force F_{max} can be estimated. For distance d greater than 0.01 cm, F_{max} exhibits monotonic increase with respect to d. Thus, increasing d is an effective strategy to enhance the overall lift generated by the ion-propelled flying microrobot. However, the drawback of excessively increasing the distance d lies in the requirement of a higher inception voltage and the adverse effects on flight stability due to the elevated center of gravity and elongation of the structure in the vertical direction. In this study, the distance d was set to 10 mm to achieve a balance between lift enhancement and maintaining flying stability.

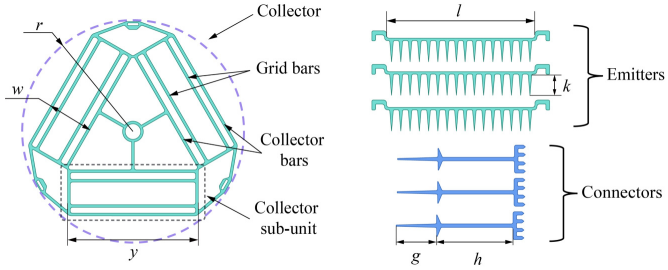

Fig. 2. Design diagrams of all components of the ion-propelled flying microrobot.

Regarding structure design, we aim to optimize ion-propelled flying microrobot performance through simulation analysis and experimental guidance. The designed microrobot consists of three emitters, a collector, and three connectors. Fig. 2 displays the component design diagrams, and Table I lists their dimensions. Three emitter-collector pairs (made from 50 μm Al-PET) arranged in an equilateral triangle configuration provide six degrees-of-freedom (DOF) flight control when independently controlled. The 30 mm long emitter has a spaced row of tip arrays, with each 4 mm long tip having a 10 degree angle to facilitate stable ionic wind generation from sharp-tip discharges at reduced potential differences. Three electrically insulated connectors, cut from 100 μm thin polyvinyl chloride (PVC) film, join the emitters and collector. Each 8 mm wide collector sub-unit has a 10 mm distance (d=h−k) between the tip and collector. The overall flying

microrobot fits within a 20 mm radius circle. A 0.3 mm unified line width for the collector is constrained by the manufacturing accuracy limit.

TABLE I. STRUCTURE PARAMETER

Parameter	Value
Width of collector sub-unit w	8 mm
Length of collector sub-unit y	24 mm
Radius of circumscribed circle r	20 mm
Length of emitter l	30 mm
Length of tip k	4 mm
Ground clearance g	4 mm
Gap between emittor and collector h	14 mm
Distance between tip and collector $d=h-k$	10 mm
Angle of tips β	10°

The development flowchart for the ion-propelled flying microrobot is shown in Fig. 3. A DIY cutting machine (Cricut Maker III, USA) was used to cut the commercially available Al-PET thin film and PVC insulating thin film. Al-PET thin film offers several advantages over metal foil or silicon when used in the construction of ion-propelled flying microrobots. One notable advantage is the significantly lower density of this material (1.38 g/cm³) compared to metal foils or silicon (2.3~8.0 g/cm³). This difference in density plays a crucial role as it reduces the overall mass of the microrobot itself, resulting in a higher thrust-to-weight ratio. Consequently, there is an increased capability to accommodate and carry onboard electronics.

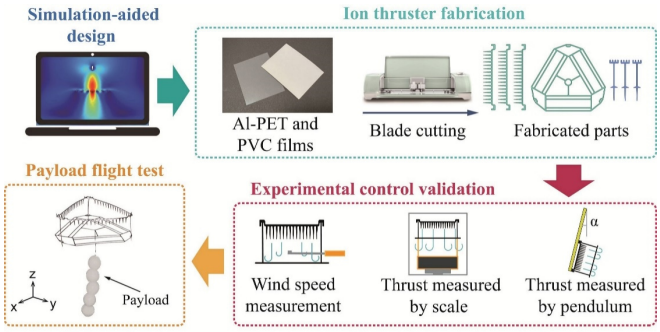

Fig. 3. Development flowchart for the ion-propelled flying microrobot.

Another advantage lies in the properties of the parts made from silicon and metals, which pose challenges in terms of precision assembly due to either difficulty in restoration or susceptibility to breakage after undergoing bending or deformation. In contrast, PET has a much lower Young's modulus (2~4 GPa) compared to Al (68~79 GPa) or silicon (130~190 GPa). This characteristic enables convenient assembly and provides robustness against unexpected impacts, enhancing the practicality of the flying microrobot. It allows for flexibility without compromising structural integrity, ensuring the longevity and reliability of the system. The emitters and collector were assembled together and bonded at their connecting positions using UV-curable epoxy. A high voltage DC power supply (Dongwen DW-P503-4ACD2, China) powered the assembled microrobot through 0.01 mm diameter enameled wires attached with carbon conductive adhesive. To enhance performance, different test assemblies with varied designs were fabricated and experimentally validated using diverse testing strategies. It is worth noting that the proposed flying microrobot features ultralow cost (under 0.1 USD) and rapid assembly (less than 10 minutes).

III. SIMULATION ANALYSIS

A. Width Optimization

We utilized FEA to model and qualitatively analyze ion generation and ion-air interactions under an applied electric field in order to examine the resultant wind speed profile and ionic thrust produced. By conducting steady-state simulations of the collector stage with different distance d between the tip and collector, the trend of wind changes is traceable while the maximum wind speed V_{max} and the average wind speed V_{avg} can also be obtained. The models of the designed ion-propelled flying microrobots were imported into COMSOL Multiphysics, and the parameters used in simulation are shown in Table II. The physical fields applied include electrostatics, laminar flow, and transport of diluted species (TDS). The ion-air interactions can be modeled and quantitatively calculated in the simulation by incorporating a Coulombic force to represent the volume force applied by ions on the air molecules [22].

TABLE II. SIMULATION PARAMETER

Parameter	Value
Diffusion coefficient	5.3×10^{-5} m²/s
Relative permittivity of air	1
Coefficient of ion mobility	$1.8\sim2.2 \times 10^{-4}$ m²/V·s
Charge number	1
Density of air	1.2 kg/m³
Heat capacity of air	1.005 kJ/kg·K
Thermal conductivity of air	25×10^{-3} W/m·K

The simulation outcome is predicated upon a controllable electric field intensity [27, 28]. An applied potential difference that generates stable ionic wind enables the steady-state solver to determine the wind speed profile, maximum wind speed and average wind speed. Cross-sectional simulations of the emitter-collector pairs are performed to obtain corresponding wind speeds for widths w ranging from 2 mm to 11 mm, as shown in Fig. 4(a)-(e). Observations show an excessively small collector width w obstructs ionic wind flow at the collector bars, reducing overall wind speed below the collector, aligning with reference [29]. On the other end of the spectrum, when the width w is excessively large, generating a stable airflow through corona discharge becomes more difficult, since the distance between the emitter tip and the collector grid increase, as shown in Fig. 4(e). Consequently, the width w must be tuned in an optimal range to maximize the wind speed. The simulation results indicate an 8 mm width w optimizes ionic wind speed, achieving a maximum of 1.69 m/s and an average of 1.14 m/s, as shown in Fig. 4(d). Given these results, an 8 mm width w was selected for our design.

B. Grid Optimization

After optimizing collector width w, another consideration is the introduction of grid structures within the collector to facilitate more ion discharges, thereby increasing the ionic wind speed [30-32]. As shown in Fig. 4(f)-(h), the wind speed for different grid structures of the collector was investigated through simulations. It was observed that incorporating two additional grid bars nearer the edge of the emitter-collector pair effectively enhanced wind speed or improved convergence of the ionic airflow. The wind speed profile including two additional grid bars positioned with a separation of 5 mm exhibited a maximum speed of 2.18 m/s and an

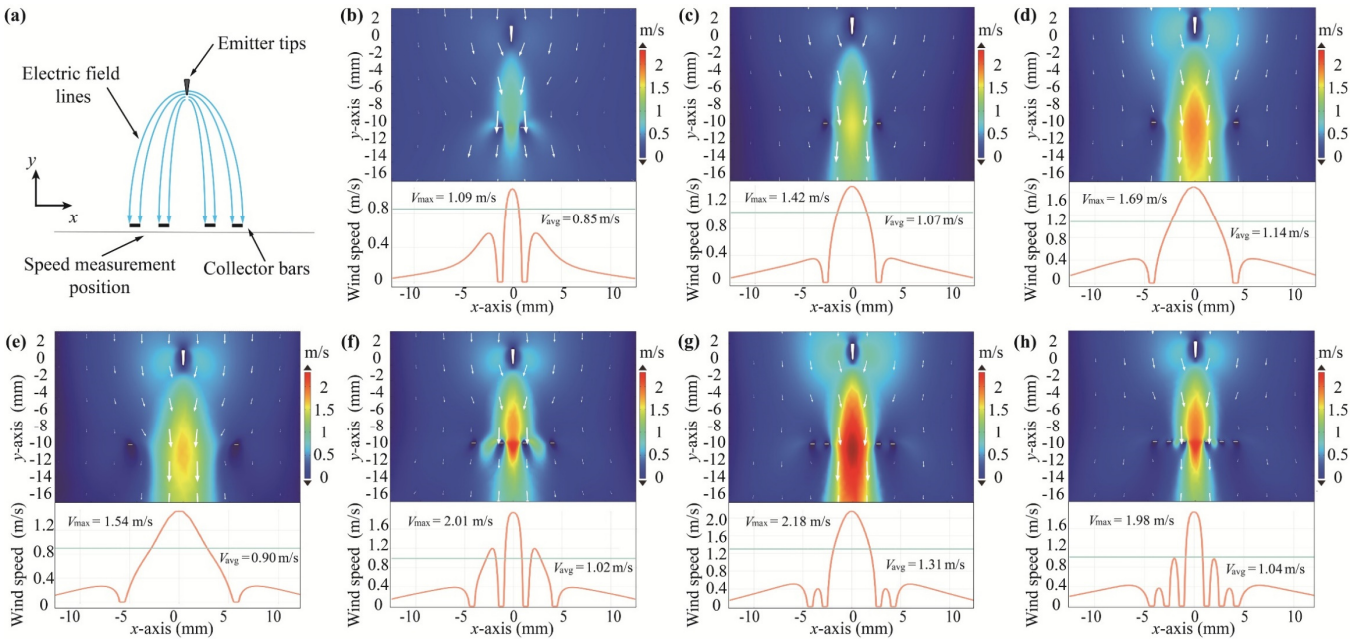

Fig. 4. (a) Simulation model. Wind velocity vector fields and profiles at $y = -10$ mm for a width w of (b) 2 mm, (c) 5 mm, (d) 8 mm, and (e) 11 mm. Wind velocity vector fields and profiles at $y = -10$ mm for the inclusion of two additional bars with a separation of: (f) 2 mm and (g) 5 mm, and (h) for the inclusion of four additional bars with separations of both 2 mm and 5 mm.

average speed of 1.31 m/s (Fig. 4(g)). However, positioning additional grid bars with a separation of 2 mm could cause disruption and constriction of airflow (Fig. 4(f)). Increasing the quantity of grid bars would also obstruct the produced ionic wind, with most of the airflow becoming constrained around the central region. In comparison to a collector lacking these grid bars, incorporating these grid bars boosted the maximum ionic wind speed by nearly 30%. Based on the identified maximum ionic wind speed of 2.18 m/s and the maximum average speed of 1.31 m/s across all the study scenarios, we have selected the structure depicted in Fig. 4(g) for the design.

IV. Experimental Verification

A. *Ion thruster testing*

We validated the FEA simulation through experimental testing of the emitter-collector pair, which consists of one emitter and a sub-unit of the collector. By measuring current and wind speed in operation, we can indirectly qualify the magnitude of ionic wind generated by thruster. The collector sub-units, with varying intervals ranging from 2~14 mm, were categorized into five groups, each incrementing by 3 mm. Current measurements with applied voltage were conducted for these groups. The gap h between the emitter and the collector sub-units was maintained at 10 mm. For each interval group, three sets of data were recorded, and their average values are shown in the Fig. 5(a). The current due to corona discharge was only generated when the voltage between the emitter and collector exceeded the inception voltage V_0. A larger distance between the collector bars implied a longer actual distance between the electrodes, thereby requiring a higher inception voltage V_0. The measurement of the ionic wind speed was conducted in a closed box because the wind speed can be easily influenced by environmental disturbance. The airflow generated by the thrusters with different designs was measured using an anemometer (Testo 405i, Germany), as shown in Fig. 5(b). A precise stage was employed to adjust the distance between the emitter and the collector with a 1 mm increment, allowing us to establish the relationship between current and wind speed. A maximum average wind speed of 1.65 m/s was achieved at 8000 V when the width w between each collector bar was set to 8 mm.

When the ion thruster was fixed on a platform, the assessment of the magnitude of the ionic wind generated can be reflected by the reduction in the total weight due to the lift generated by the thrust. By employing this approach, the correlation between the weight loss and the voltage can be quantified through the utilization of a precision balance (XIULAB FA2204, China). The ion thruster was positioned with adequate clearance to prevent the ionic wind from

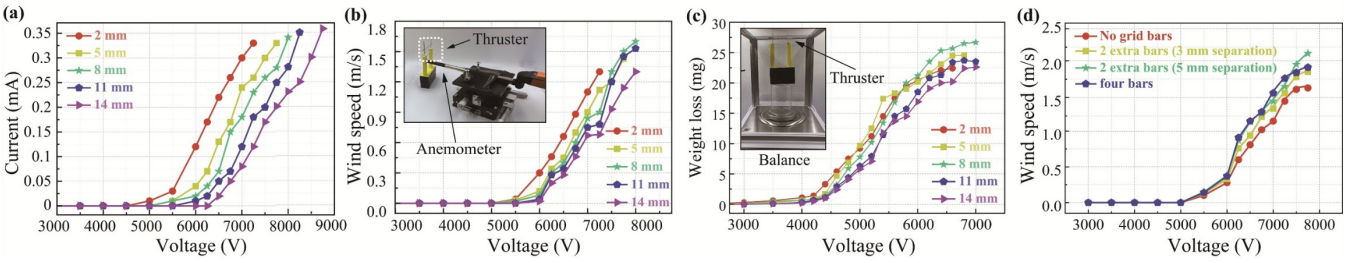

Fig. 5. (a) Current, (b) wind speed and (c) weight loss corresponding to the voltage as collector widths range from 2 mm to 14 mm. (d) Wind speed corresponding to the voltage for different grid bar configurations. Insets: Photos of the experimental setups.

impacting the platform. To minimize measurement errors from electrostatic interference, the precision balance surface was covered with a thin PVC film coated with antistatic paint. The experiment was conducted in a confined environment to exclude external airflows since the mass loss was minute and the measurement was susceptible to instability from ambient airflows. As can be seen from Fig. 5(c), the experiments revealed the peak mass loss was achieved with a separation of 8 mm between the grid bars, amounting to 27 mg. The total weight of the ion thruster was 5 mg, resulting in a thrust-to-weight ratio of approximately 5.4.

In addition to finding the optimal width *w*, this work also explored the experimental validation of the grid configuration of the collector. By comparing the effects of five different designs on ionic wind speed in the ion thruster experiment, it was found that adding two grid bars, each positioned 1.5 mm away from the frame, achieves the maximum wind speed of approximately 2.25 m/s (Fig. 5(d)). This value agreed with the simulation results mentioned earlier. Moreover, the wind speed measurement also showed that the thrust with four grid bars better focuses and intensifies the ionic airflow direction, increasing wind velocity. However, excessive grid bars can impede airflow and consequently decrease the thrust.

To visually demonstrate the EHD force, an experiment was conducted to measure deflection of a wooden pendulum caused by the ionic wind. As shown in Fig. 6(a), by mounting the ion thruster at the bottom of a wooden rod and applying voltage, the amplitude of the induced deflection can be measured to determine the magnitude of the EHD force and calculate the thrust-to-weight ratio generated by the thruster. Tip density is used to refer to the ratio between the number of emitter tips and the maximum number of tips that would exist if the tips were fully distributed along the length of the emitter. By comparing thrust deflections at various tip densities, Fig. 6(b) illustrates the maximum deflection of 90 mm achieved with 100% tip density. With the 1 m rod length and 288.9 mg weight, this translated to a thrust-to-weight ratio of 5.2. The wind speeds decreased progressively for emitters with 50% and 25% tip densities, aligning with ion generation principles. Specifically, applied voltage caused ions to emit from the tips, so a higher number of tips generates stronger ionic winds.

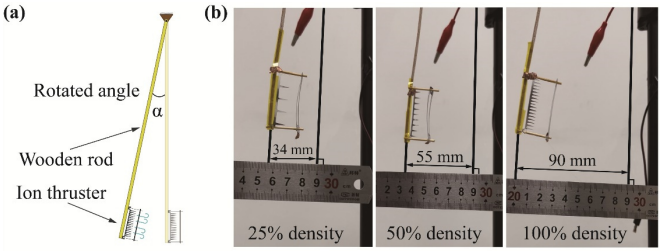

Fig. 6. (a) Schematic illustration and (b) photos of thrust measurement via deflection of a wooden pendulum using emitters with varied tip densities.

Additionally, visual smoke studies qualitatively demonstrated voltage effects on flow fields around the thruster. With no applied voltage, low-velocity smoke streams from a left-side smoke pipe remained near-horizontal when traversing the thruster (Fig. 7(a)). In contrast, when subjected to voltage (Fig. 7(b)), the smoke streams deflected downwards through the thruster, reflecting the airflow direction generated by the thruster (Movie S1). Clearly, the airflow was so intense that hardly any smoke streams can pass through the thruster.

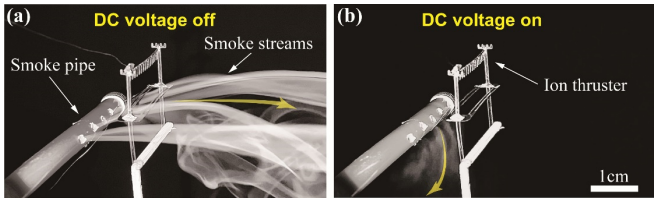

Fig. 7. Visualization of the airflow (a) in the absence and (b) in the presence of corona discharge.

B. *Flight Demonstration with Payload*

As demonstrated in Fig. 8, stable flight of the developed ion-propelled flying microrobot was achieved while carrying payloads substantially exceeding its own weight. The takeoff and elevation of a flying microrobot were intricately governed by the regulation of the applied voltage. Once applied voltage surpassed the threshold voltage and continued to escalate, thrusters initiated an ionic wind, gradually enabling it to take off and hover. Furthermore, by increasing the applied voltage, the microrobot's flight altitude can effectively be elevated. The symmetrically arranged enameled wire (0.01 mm in diameter) for voltage supply decreased the tilting tendency of the flying microrobot, ensuring a smooth vertical takeoff and enabling precise elevation control within a specific range of altitudes. In the flight experiment, the flying microrobot successfully reached a notable maximum vertical flight height of approximately 170 mm without any payload. At this peak altitude, the flying microrobot exhibited stability and maintained stable hovering. Furthermore, to showcase the flying microrobot's maximum AUW capacity, a flight demonstration involved affixing five foam balls as the payload to the lower side of the microrobot (Fig. 8, Movie S2). With the microrobot weighing just 16 mg, vertical takeoff and landing were successfully achieved even while carrying payloads weighing up to 72 mg total (4.5 times the flying microrobots' weight). Thus, the thrust-to-weight ratio of the tested microrobot reached up to 5.5. Relative to prior literature, the ion-propelled flying microrobot engineered in this work enhanced the thrust-to-weight ratio while achieving an ultralow weight, as depicted in Fig. 9. The experimental demonstration verified the microrobot's capability not only to support its own weight for sustained flight but also to lift and transport payloads exceeding its own weight multiple times over, unveiling potential for integrating additional various electronics to enable autonomous operation in future iterations.

V. Conclusion

This research paper presents an exploration of the design, simulation, testing, and flight of an ion-propelled flying microrobot, shedding light on its potential characteristics and applications. The microrobot, weighing a mere 16 mg, demonstrates a promising thrust-to-weight ratio (>5), making it one of the lightest and most capable flying microrobots in its class. The cost-effective manufacturing process, with a production cost of less than 0.1 USD, is an encouraging aspect for scalability and mass production. Through the implementation of an optimized structure design, informed by FEA considering electrical field, fluid field, and particle motion, insights into the optimal structural design of ion-propelled flying microrobots have been obtained. Furthermore, the utilization of an optimized structural material, the Al-coated PET thin film, a metal-polymer combined material,

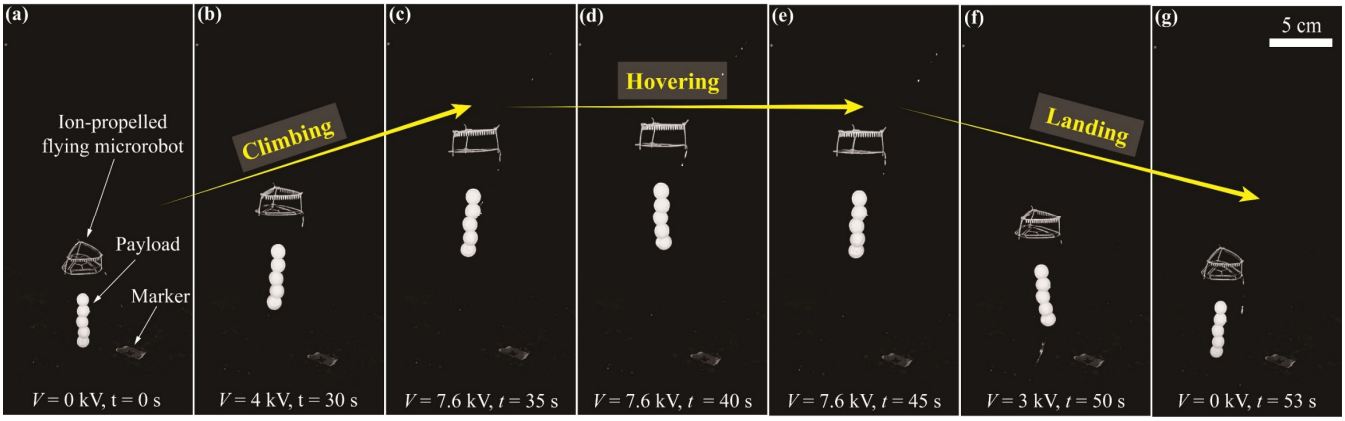

Fig. 8. Flight state images of the ion-propelled flying microrobot carrying a payload. (a) and (g) display the initial and final states, respectively. (a)-(c) and (e)-(g) display the ascending and descending states, respectively. (c)-(e) display the hovering states.

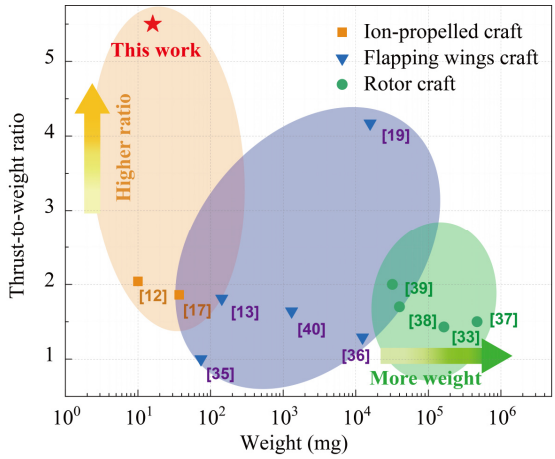

Fig. 9. Comparison of thrust-to-weight ratio and weight in reported research.

showcases the ability to reduce weight while enhancing robustness. This material selection not only mitigates fabrication and assembly difficulties but also minimizes production time, facilitating mass production of the microrobot. The experimental testing of the corona discharge-induced EHD force, which serves as the optimized thruster for the flying microrobot, has been conducted through two different methods using an electric balance and a mechanical pendulum. The deflection of the wooden rod in the pendulum experiment directly reflects the thrust generated by the ionic wind. Additionally, visual smoke studies qualitatively demonstrate voltage effects on flow fields surrounding the thruster. Comprehensive simulations and experimental studies have resulted in the successful manufacture of a flying microrobot weighing only 16 mg, with a payload capacity of 72 mg. The flight experiments affirm the microrobot's ability to not only support its own weight for sustained flight but also lift payloads exceeding five times its own weight.

While the current design requires wired connections to provide the necessary potential difference for stable flight within a limited range and the presence of strong winds and intense magnetic interference may give rise to uncontrollable disturbances, it presents a promising avenue for future applications. This design offers possibilities such as suspending microelectronics, hovering, and vertical take-off and landing, opening up avenues for the development of autonomous ion-propelled flying microrobots. Rapid advance in wireless power transmission or onboard power generation technologies could overcome the limitations of wired connections and enable extended range and untethered flight. The fusion of these technological advancements, enabling fully autonomous flying robots, harbors potential to drive progress in multiple domains, such as aerial inspection, surveillance, environmental monitoring, and more.

ACKNOWLEDGMENT

The authors gratefully acknowledge support from the National Science Foundation under grants EPSCoR-2119485, Jiangsu Specially-Appointed Professor Program, and Natural Science Research Start-up Foundation of Nanjing University of Posts and Telecommunications.

REFERENCES

[1] Y. Chen, H. Zhao, J. Mao, P. Chirarattananon, E. F. Helbling, N. P. Hyun, D. R. Clarke, and R. J. Wood, "Controlled flight of a microrobot powered by soft artificial muscles," *Nature*, vol. 575, no. 7782, pp. 324-329, 2019.

[2] S. J. Carlson, P. Arora, T. Karakurt, B. Moore, and C. Papachristos, "Towards multi-day field deployment autonomy: A long-term self-sustainable micro aerial vehicle robot," in *2023 IEEE International Conference on Robotics and Automation (ICRA)*. IEEE, 2023, pp. 11396-11403.

[3] D. Floreano and R. J. Wood, "Science, technology and the future of small autonomous drones," *Nature*, vol. 521, no. 7553, pp. 460-466, 2015.

[4] W. Gao, H. Haitjema, F. Z. Fang, R. K. Leach, C. F. Cheung, E. Savio and J. M. Linares. "On-machine and in-process surface metrology for precision manufacturing," *CIRP Annals*, vol. 68, no. 2, pp. 843-866, 2019.

[5] A. Fath, T. Xia, and W. Li. "Recent Advances in the Application of Piezoelectric Materials in Microrobotic Systems," *Micromachines*, vol. 13, no. 9, pp. 1422, 2022.

[6] N. O. Lambert, C. B. Schindler, D. S. Drew, and K. S. J. Pister, "Nonholonomic Yaw Control of an Underactuated Flying Robot With Model-Based Reinforcement Learning," *IEEE Robotics and Automation Letters*, vol. 6, no. 2, pp. 455-461, 2021.

[7] S. Bai, R. Ding, and P. Chirarattananon, "A Micro Aircraft with Passive Variable-Sweep Wings," in *IEEE Robotics and Automation Letters*, vol. 7, no. 2, pp. 4016-4023, 2022.

[8] D. S. Drew and K. S. J. Pister, "First takeoff of a flying microrobot with no moving parts," in *2017 International Conference on Manipulation, Automation and Robotics at Small Scales (MARSS)*. IEEE, 2017, pp. 1-5.

[9] D. Drew, D. S. Contreras, and K. S. J. Pister, "First thrust from a microfabricated atmospheric ion engine," in *2017 IEEE International Conference on Micro Electro Mechanical Systems (MEMS)*. IEEE, 2017, pp. 346-349.

[10] L. Young, E. Aiken, J. Johnson, R. Demblewski, J. Andrews, and J. Klem, "New concepts and perspectives on micro-rotorcraft and small autonomous rotary-wing vehicles," in *2002 AIAA Applied Aerodynamics Conference*. AIAA, 2002, pp. 2816.

[11] S. Lai, K. Wang, H. Qin, J. Q. Cui, and B. M. Chen, "A robust online path planning approach in cluttered environments for micro rotorcraft drones," *Control Theory and Technology*, vol. 14, pp. 83-96, 2016.

[12] F. Bohorquez, P. Samuel, J. Sirohi, D. Pines, L. Rudd, and R. Perel, "Design, analysis and hover performance of a rotary wing micro air vehicle," *Journal of the American Helicopter Society*, vol. 48, no. 2, pp. 80-90, 2003.

[13] S. B. Fuller, "Four wings: An insect-sized aerial robot with steering ability and payload capacity for autonomy," *IEEE Robotics and Automation Letters*, vol. 4, no. 2, pp. 570-577, 2019.

[14] X. Yan, M. Qi, and L. Lin, "Self-lifting artificial insect wings via electrostatic flapping actuators," in *2015 IEEE International* Conference *on Micro Electro Mechanical Systems (MEMS).* IEEE, 2015, pp. 22-25.

[15] K. Y. Ma, P. Chirarattananon, S. B. Fuller, and R. J. Wood, "Controlled flight of a biologically inspired, insect-scale robot," *Science*, vol. 340, no. 6132, pp. 603-607, 2013.

[16] C. F. Chung and W. J. Li, "Experimental studies and parametric modeling of ionic flyers," in *2007 IEEE/ASME international conference on advanced intelligent mechatronics (AIM)*. IEEE, 2007, pp. 1-6.

[17] H. K. H. Prasad, R. S. Vaddi, Y. M. Chukewad, E. Dedic, I. Novosselov, and S. B. Fuller, "A laser-microfabricated electrohydrodynamic thruster for centimeter-scale aerial robots," *PloS one,* vol. 15, no. 4, p. e0231362, 2020.

[18] D. S. Drew, N. O. Lambert, C. B. Schindler, and K. S. J. Pister, "Toward controlled flight of the ionocraft: a flying microrobot using electrohydrodynamic thrust with onboard sensing and no moving parts," *IEEE Robotics and Automation Letters*, vol. 3, no. 4, pp. 2807-2813, 2018.

[19] T. Roelandt and D. Vandepitte, "Inherently stable descending flight of a tailless flapping wing micro air vehicle by upward wing elevation," *International Journal of Micro Air Vehicles*, vol. 15, p. 17568293231178263, 2023.

[20] D. B. Go, R. A. Maturana, T. S. Fisher, and S. V. Garimella, "Enhancement of external forced convection by ionic wind," *International Journal of Heat and Mass Transfer*, vol. 51, no. 25-26, pp. 6047-6053, 2008.

[21] H. Xu, Y He, K. L. Strobel, C. K. Gilmore, S. P. Kelley, C. C. Hennick, T. Sebastian, M. R. Woolston D. J. Perreault, and S. R. H. Barrett, "Flight of an aeroplane with solid-state propulsion," *Nature*, vol. 563, no. 7732, pp. 532-535, 2018.

[22] N. Guettaf, Z. Anane, S. el islem Guettaf, F. Hassaine, and H. Nouri, "Study of the different parameter corona discharge in point-plane Electrostatic Separator," in *2022 IEEE International Multi-Conference on Systems, Signals & Devices (SSD)*. IEEE, 2022, pp. 1831-1835.

[23] P. Cooperman, "A theory for space-charge-limited currents with application to electrical precipitation," *Transactions of the American Institute of Electrical Engineers. Part I: Communication Electronics*, vol. 79, no. 1, pp. 47-50, 1960.

[24] M. Robinson, "Movement of air in the electric wind of the corona discharge," *Transactions of the American Institute of Electrical Engineers, Part I: Communication and Electronics*, vol. 80, no. 2, pp. 143-150, 1961.

[25] M. A. Lieberman and A. J. Lichtenberg, "Principles of plasma discharges and materials processing," *MRS Bulletin*, vol. 30, no. 12, pp. 899-901, 1994.

[26] Y. P. Raizer and J. E. Allen, Gas discharge physics. Springer, 1991.

[27] N. E. Jewell-Larsen, C. P. Hsu, I. A. Krichtafovitch, S. W. Montgomery, J. T. Dibene, and A. V. Mamishev, "CFD analysis of electrostatic fluid accelerators for forced convection cooling," *IEEE Transactions on Dielectrics and Electrical Insulation*, vol. 15, no. 6, pp. 1745-1753, 2008.

[28] H. M. S. Aaron, "Efficiency of Electric to Kinetic Energy Conversion of an Electrohydrodynamic Thruster in a Moving Bulk-Fluid," *in 2021 IEEE KhPI Week on Advanced Technology (KhPIWeek)*. IEEE, 2021, pp. 168-171.

[29] E. Defoort, R. Bellanger, C. Batiot-Dupeyrat, and E. Moreau, "Ionic wind produced by a DC needle-to-plate corona discharge with a gap of 15 mm," *Journal of Physics D: Applied Physics*, vol. 53, no. 17, p. 175202, 2020.

[30] Z. He and E. T. M. Dass, "Correlation of design parameters with performance for electrostatic Precipitator. Part I. 3D model development and validation," *Applied Mathematical Modelling*, vol. 57, pp. 633-655, 2018.

[31] C. K. Gilmore and S. R. H. Barrett, "Electrohydrodynamic thrust density using positive corona-induced ionic winds for in-atmosphere propulsion," *Proceedings of the Royal Society A: Mathematical, Physical and Engineering Sciences*, vol. 471, no. 2175, p. 20140912, 2015.

[32] Z. Feng, Z. Long, S. Cao, and K. Adamiak, "Characterization of electrohydrodynamic (EHD) flow in electrostatic precitators (ESP) by numerical simulation and quantitative vortex analysis," *Journal of Electrostatics*, vol. 91, pp. 70-80, 2018.

[33] S. Bouabdallah, P. Murrieri, and R. Siegwart, "Design and control of an indoor micro quadrotor," in *IEEE International Conference on Robotics and Automation (ICRA)*. IEEE, 2004, pp. 4393-4398.

[34] J. S. Patel, C. Al-Ameri, F. Fioranelli, and D. Anderson, "Multi-time frequency analysis and classification of a micro-drone carrying payloads using multistatic radar," *The Journal of Engineering*, vol. 2019, no. 20, pp. 7047-7051, 2019.

[35] Y. M. Chukewad, J. James, A. Singh, and S. B. Fuller, "RoboFly: An insect-sized robot with simplified fabrication that is capable of flight, ground, and water surface locomotion," *IEEE Transactions on Robotics* vol. 37, no. 6, pp. 2025-2040, 2021.

[36] T. Ozaki, N. Ohta, T. Jimbo, and K. Hamaguchi, "Ta Liftoff of A Untethered Tailless Flapping-Wing Micro Aerial Vehicle With Integrated Battery," *IEEE Robotics and Automation Letters*, vol. 8, no. 6, pp. 3574-3580, 2023.

[37] J. F. Shepherd III and K. Tumer, "Robust neuro-control for a micro quadrotor," in *Proceedings of the 12th annual conference on Genetic and evolutionary computation (GECCO)*. SIGEVO, 2010, pp. 1131-1138.

[38] S. K. Phang, K. Li, K. H. Yu, B. M. Chen, and T. H. Lee, "Systematic design and implementation of a micro unmanned quadrotor system," *Unmanned Systems*, vol. 2, no. 02, pp. 121-141, 2014.

[39] J. Yoo, D. Jang, H. J. Kim, and K. H. Johansson, "Hybrid Reinforcement Learning Control for a Micro Quadrotor Flight," *IEEE Control Systems Letters*, vol. 5, no. 2, pp. 505-510, 2021.

[40] T. Ozaki, N. Ohta, T. Jimbo, and K. Hamaguchi, "Takeoff of a 2.1 g Fully Untethered Tailless Flapping-Wing Micro Aerial Vehicle With Integrated Battery," *IEEE Robotics and Automation Letters*, vol. 8, no. 6, pp. 3574-3580, 2023.